Tailored self-assembled nanocolloidal Huygens scatterers in the visible

Rajam Elancheliyan, Romain Dezert, Sabine Castano, Ahmed Bentaleb, Einat Nativ- Roth, Oren Regev, Philippe Barois, Alexandre Baron, Olivier Mondain-Monval, Virginie Ponsinet

Tailored self-assembled nanocolloidal Huygens scatterers in the visible†

Rajam Elancheliyan,[a] Romain Dezert,[a] Sabine Castano,[b] Ahmed Bentaleb,[a] Einat Nativ-Roth,[c] Oren Regev,[c,d] Philippe Barois,[a] Alexandre Baron,*[a] Olivier Mondain-Monval[a] and Virginie Ponsinet*[a]

Abstract: Existing nanocolloidal optical resonators presenting strong magnetic resonances often suffer from multi-step low yield synthesis routes as well as a limited tunability, in particular in terms of spectral superposition of electric and magnetic resonances, which is the cornerstone for achieving Huygens scatterers. To overcome these drawbacks, we have synthesized clusters of gold nanoparticles using an emulsion-based formulation route. The fabrication technique involved the emulsification of an aqueous suspension of gold nanoparticles in an oil phase, followed by the controlled ripening of the emulsion. The structural control of the as-synthesized clusters, of mean radius 120 nm and produced in large numbers, is demonstrated with microscopy and X-ray scattering techniques. Using a polarization-resolved multi-angle light scattering setup, we reach a comprehensive angular and spectroscopic determination of their optical resonant scattering in the visible wavelength range. We thus report on the clear experimental evidence of strong optical magnetic resonances and directional forward scattering patterns. The clusters behave as strong Huygens sources. Our findings crucially show that the electric and magnetic resonances, as well as the scattering patterns can be tuned by adjusting the inner cluster structure, playing with a simple parameter of the fabrication route. This experimental approach allows for the large scale production of nanoresonators with potential uses for Huygens metasurfaces.

1 Introduction

Tailoring the scattering properties of individual nanostructures is paramount to many nanophotonic applications. Indeed, it drives the efficiency of devices that aim at controlling electromagnetic waves both in phase and in amplitude over nanoscale dimensions. Metasurfaces and flat optical systems for instance are two-dimensional devices that fulfill an optical function with an ensemble of nanoscatterers arranged into a single layer. Many functions have been demonstrated or proposed that include lensing[1], perfect absorption[2,3], imaging, holography[4], polarization control[5], wavefront control[6] or bio-sensing[7] to name a few. As a result, they require nanostructures with specific individual scattering properties, two of which are certainly the most important. The first important property is that the nanoobjects should be low-loss forward scatterers. This ensures that a metasurface composed of these nanoscatterers will exhibit a near-unity transmissivity. The second important property is that the scattering efficiency should be large. This ensures that a significant portion of the incident flux will be affected and as a consequence, the larger the scattering efficiency, the less dense the metasurface need to be. Such nanoobjects are called Huygens scatterers and the flat optical devices that use them are called Huygens metasurfaces[6,8,9] in reference to the Huygens-Fresnel principle[10]. This principle is a mathematical statement considering every point on a wavefront as a source of hemispherical wavelets that are emitted in the forward direction. In the last decade, it was realized that such Huygens scatterers could be achieved by exploiting the multipole resonances of a nanoparticle. Initially the superposition both in phase and in amplitude of an electric and a magnetic dipole resonances was targeted[6,11]. Such a superposition ensures that the scattering occurs in the forward direction only. If the scattering

[a] *Univ. Bordeaux, CNRS, Centre de Recherche Paul Pascal, UMR 5031, F-33600 Pessac, France, E-mail: alexandre.baron@u-bordeaux.fr, virginie.ponsinet@crpp.cnrs.fr*
[b] *Institut de Chimie et Biologie des Membranes et des Nano-objets, Univ. Bordeaux, CNRS, INP, UMR 5248, F-33600 Pessac, France.*
[c] *Department of Chemical Engineering, Ben Gurion University of the Negev IL-84105 Beer Sheva, Israel.*
[d] *Ilse Katz Institute for Nanoscale Science and Technology, Ben Gurion University of the Negev IL-84105 Beer Sheva, Israel.*
† Electronic Supplementary Information (ESI) available: [Supplementary Information present TEM characterization of the nanoparticles and clusters, ATR-FTIR demonstration of the water evaporation during emulsion ripening, simulations of the multipolar decomposition of the clusters scattering cross-section, and the experimental plots of the perpendicular and parallel scattering signals, shown as an example for one sample at a given wavelength.]. See DOI: 00.0000/00000000.

efficiency is large enough – say close to unity – then a metasurface composed of these scatterers may impart a 2π variation of the phase across the spectral range of the dually resonant system. Recently, it was realized that, when the dipolar approximation does not hold, a Huygens scatterer could be achieved by getting the superposition of odd multipoles to be equal to that of even multipoles[5]. Such system is sometimes referred to as a generalized Kerker source[12].

Huygens scatterers demonstrated thus far are anisotropic and directly fabricated lithographically in a two-dimensional layer[1,6,8,9,11]. Furthermore, none have been demonstrated in the visible range. In stark contrast, self-assembly routes offer a promising alternative[13,14] by being well adapted to nanostructures responding in the visible wavelength range and by making it possible to separate the scatterer fabrication from the metasurface assembly. As a result, designing and fabricating the Huygens scatterers can be done irrespective of the Huygens metasurface applications and they may come in vast amounts in the form of inks composed of colloidal suspensions.

A Huygens nanoscatterer may be achieved with a homogeneous nanosphere of index n immersed in a host medium of index n_h. The scattering efficiency is defined as the ratio of the scattering cross-section to the geometric cross-section. The most efficient a homogeneous Huygens scatterer can be for a lossy medium is when $n/n_h = 2.0 + 0.095i$[15]. Increasing the index of refraction beyond this value will spectrally separate the resonant multipoles and destroy the forward-scattering property. Dezert *et al.* proposed not only that realistically achievable colloidal nanoclusters made of ensembles of plasmonic or dielectric nanoparticles (NPs) could reach this homogeneous regime of ideal Huygens scattering in the visible, but also that they had the potential to surpass it by exhibiting larger efficiencies than those achievable in the homogeneous limit[15].

Following this proposal, we consider nanoclusters made by the colloidal self-assembly of gold plasmonic NPs to produce strong and tailored Huygens nanoscatterers in the visible. This design was already proposed theoretically by Rockstuhl *et al.*[16] and explored experimentally[17,18] to produce effective Mie scatterers with optical magnetism. It consists in an assembly of N NPs of radius r distributed quasi-homogeneously within the spherical volume of radius R of a cluster.

Assembly of NPs into dense clusters has been studied via different colloidal engineering routes, using block copolymer self-assembly[19,20], hydrophobic interactions[21], specific ligand association[18,22], or electrostatic assembly[23,24], for example. We chose to use an inverse emulsion ripening process via dehydration of water droplets containing the gold NPs, which is a potentially large-scale process. The confinement of nanoparticles in emulsion droplets, followed by their controlled shrinkage by either Ostwald ripening or evaporation, has been considered a powerful way to control their assembly both for a small[25–27] or for a large[28–30] number N of NPs in the final clusters. We focused on tailoring the emulsion formulation to control the cluster mean radius R and the volume fraction $f = N(r/R)^3$ of gold NPs within the clusters, in order to tune their optical response and reach a strong and isotropic Huygens scattering regime.

The paper is organized as follows. First, we present the chosen emulsion system and its controlled ripening, then the final cluster structure, and finally the measured spectral and angular scattering properties of the clusters that demonstrate the Huygens property.

2 Results and discussion

2.1 Initial emulsion

Several aqueous gold NPs suspensions were prepared as explained in the Experimental Section below and used as the dispersed phase in the emulsion with a gold volume fraction of 4×10^{-6}. The NPs consist in a gold core of mean radius 6.7 nm covered by different ligand coronas. In the suspension referred to as PVP-NPs, the corona is made of adsorbed polyvinylpyrolidone chains (M_w = 10 kg/mol) while in the suspensions named PEGX/Y-NPs, the corona is a grafted shell of methoxy poly(ethylene glycol) thiols (PEG-SH) of different molar mass M_w and of variable density: X is the molar mass of the PEG-SH ($X = 800$ g/mol, 2000 g/mol or 6000 g/mol) and Y is 10 times the number of ligand molecules per nm^2 ($Y = 5$, 10, 20 or 40 for 0.5, 1, 2 or 4 ligand molecules/nm^2, respectively). Quantifying the molecular size and density of the ligands on the NP surface, X and Y encode the quantity of organic matter wrapping each gold NP.

Suspensions of gold NPs present a strong absorption band in the visible wavelength domain, due to their localized surface plasmon resonance (LSPR), at a spectral position which depends on their size, morphology (spheres, rods, etc.) and surrounding medium. This absorption band is very sensitive to electromagnetic couplings between NPs and is therefore an indicator of their colloidal state and degree of aggregation. Figure 1.(a) shows the extinction spectrum of the gold PVP-NPs (blue curve), indicating a good colloidal stability with a narrow LSPR band at $\lambda_{NP} = 522$ nm, as expected in such conditions.

The PVP-NPs, and several PEGX/Y-NPs aqueous suspensions were each emulsified in dodecane (see Experimental

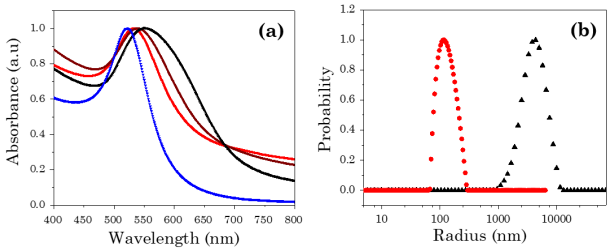

Fig. 1 (a) Normalized UV-Vis spectra of a dispersion of gold PVP-NPs in water (blue) and aliquots of the PVP-NPs emulsion after a ripening time of 60 min (red), 75 min (brown) and 75 min plus two days of stirring at atmospheric pressure (black); (b) Normalized radius distributions determined by granulometry and DLS measurements, respectively, for the size of the initial emulsion droplets (black triangles) and the final clusters obtained by ripening the PVP-NPs emulsion (red dots).

Section below) to produce droplets with sizes, measured by granulometry, ranging from $R_d = 1.5$ to 7 μm, with a most probable value of 4 μm (see an example of the size distribution in Fig. 1, black triangles). The chosen batch emulsification technique produces a rather wide size distribution but was preferred over techniques giving more monodisperse emulsions (like microfluidics for instance) for its significantly higher yield. In a typical experiment, about 2 mL of droplets were produced, leading to $\sim 10^9$ resonators/batch, which can be easily scaled up when needed. The emulsion was then ripened to evaporate the water, thus bringing the nanoparticles closer in order to obtain the final clusters.

2.2 Cluster formation

The emulsions were agitated at room temperature and kept under a pressure around 7.5 mmHg using a rotavapor device, in order to gently evaporate the water.

2.2.1 Ripening process

During the emulsion ripening process, aliquots were sampled at different intervals of time and were studied using both UV-Visible and IR spectroscopies. ATR-FTIR spectra displayed in the Supplementary Information show the decrease and eventual disappearance of initially intense water bands after typically a few hours of ripening. Figure 1.(a) shows the UV-Vis spectra of emulsion aliquots together with that of the initial gold NPs suspension. The spectra presents increasing broadening and red-shift of the absorption band as the ripening is increased. The increasing confinement of the Au NPs within the droplets of reducing size decreases the distance between particles, resulting in the occurrence of plasmonic couplings and, therefore, in a red-shift of the LSPR peak. The LSPR band remains nevertheless well-defined, which hints at a good homogeneity of the distance between NPs. This process is accompanied by a color change of the solution from pink to blue. According to Mie theory calculations (see e.g. Fig. 3 in Ref. 17), the broadening and red-shift of the plasmonic extinction band observed for the final sample are compatible with electromagnetic couplings between NPs, with an edge-to-edge distance on the order of 3 nm.

This dramatic decrease of the interparticle distance is compatible with the evolution of the global size of the objects. Fig. 1.(b) shows that the size of the initial droplets is decreased by a factor ~ 40 upon ripening, inducing a $\sim 6 \times 10^4$-fold multiplication of the internal gold volume fraction, which then reaches values typically above 0.1. Similar results were obtained with the PEG-NPs emulsions. More precisely, the dimensions of the final clusters are found by dynamic light scattering (DLS, see Experimental Section below) to be well accounted for by log-normal distributions with the natural logarithm of the clusters radius having a standard deviation of 0.15 ± 0.02 and a mean value corresponding to $R = 140$ nm for clusters PVP-NPs and $R = 120$ nm for clusters PEG6000/20-NPs, PEG2000/20-NPs and PEG800/40-NPs.

2.2.2 Evidence of interparticle correlation by SAXS.

The different PEGX/Y-NPs emulsions were studied by small-angle X-ray scattering (SAXS). Figure 2 displays (in pink squares) the SAXS signal of the initial PEG2000/10-NPs suspension before emulsification. For X-rays, the scattering length density of gold is very high compared to the one of organic compounds, either ligands or solvents, and we benefit from a high scattering contrast. Specifically, the contrast between the solvated PEG layer and water being much lower than that between solvated PEG and dense gold, the NPs signal can be modeled as that of simple homogeneous spheres. The

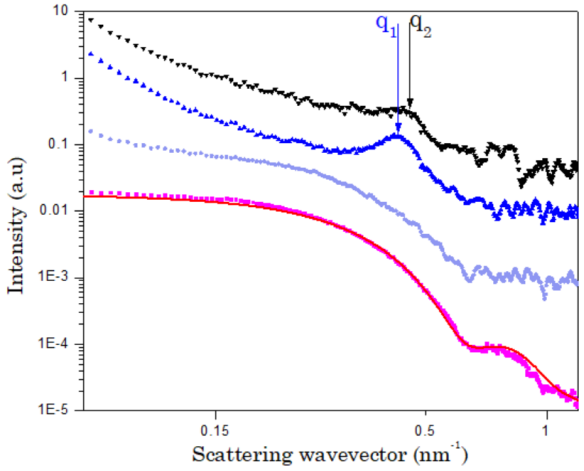

Fig. 2 SAXS signal of the initial suspension of PEG2000/10-NPs in water (pink dots), and of the PEG2000/10-NPs emulsion after 3hrs40min (light blue), 3hrs45min (dark blue) and 3hrs50min (black). The peaks are at positions $q_1 = 0.40$ nm^{-1} and $q_2 = 0.41$ nm^{-1}. The red line is the theoretical form factor of polydisperse homogeneous spheres (Equations (1) and (2)) adjusted to the NPs signal. The curves are vertically shifted for clarity. Note that the intensity of the last (3hr50min) aliquot is lower than for the previous aliquot (3hr45min) due to a loss of scatterers in the process.

continuous red line in Fig. 2 is the theoretical form factor of homogeneous dense spheres of radius r with no interactions:

$$P(q,r) = \frac{(\sin(qr) - qr\cos(qr))^2}{q^6}, \tag{1}$$

convoluted with a Gaussian size distribution

$$D(r,r_s) = \frac{1}{\sigma\sqrt{2\pi}}\exp\left(-\frac{(r-r_s)^2}{2\sigma^2}\right), \tag{2}$$

and fitted to the experimental signal as a function of the wavevector q. The adjusted mean size and standard deviation are the only adjustable parameters and are found to be $r_s = 6.7$ nm and $\sigma = 1.0$ nm, respectively, in very good agreement with TEM observations (shown in the SI Figures S1 and S2).

Aliquots extracted during the ripening of the PEG2000/10-NPs emulsion were also studied by SAXS, and Figure 2 displays the SAXS signal of the emulsion at 3hrs 40min, 3hrs 45min and 3hrs 50min (from bottom to top). During most of the ripening process as well as for the 3hrs40min aliquot, the SAXS signal is dominated by the scattering of the individual NPs. In the 3hrs40min SAXS signal, an increase of the scattered intensity at the smallest measured wavevectors can be attributed to the onset of some large-scale correlations between NPs. Clear deviation from the NPs form factor appears for the later ripening times. Peaks are visible at $q_1 = 0.40$ nm^{-1} and $q_2 = 0.41$ nm^{-1}, for 3hrs 45min and 3hrs 50min, respectively, which we interpret as due to a spatial correlation between the NPs inside the droplets.

We can note that the correlation appears quite suddenly and evolves only slightly between 3hrs 45min and the end of the ripening. The absence of such correlation at earlier stages of the ripening demonstrates that there is no uncontrolled aggregation of the NPs until the confinement of the droplet walls forces it. In other words, the NPs interact only as hard spheres, at short distance, when the confinement due to the decreasing droplet volume bring them close to each other. The absence of long-range attractive interactions between NPs is an asset to produce dense aggregates in contrast with fractal structures obtained with attractive NPs[31].

The observed interparticle correlation at the latest time corresponds to a center-to-center distance of $d_{c-c} = 2\pi/q_2 = 15.3$ nm, i.e. an edge-to-edge distance of $d_{e-e} = d_{c-c} - 2r_s = 1.9$ nm, which is a reasonable value for the thickness of the organic shell produced by the PEG ligand of molar weight 2000 g/mol. Indeed, $d_{c-c}/2$ can be equated to the radius of the NPs decorated by the dry organic ligand shell, while r_s is the radius of the bare gold spheres. The edge-to-edge distance d_{e-e} is also compatible with the interparticle distance inferred from UV-vis spectroscopy for the PVP-NPs clusters.

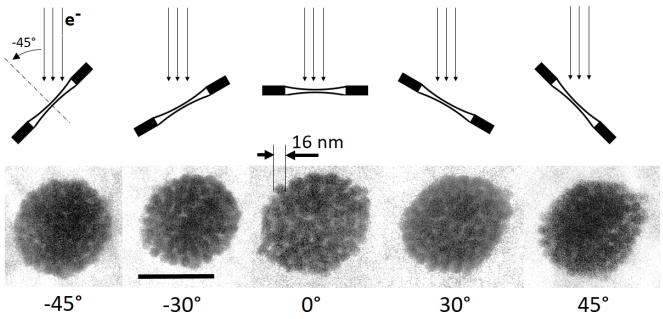

Fig. 3 Schematic representation (upper part) of how the vitrified cluster suspension film is tilted for observation. Cryo-TEM images (lower part) of a representative Au-cluster under different observation angles. The scale bar is 100 nm.

2.3 Final clusters structure

At the end of the evaporation process, the water volume fraction is below the sensitivity of the IR measurement technique, and the SAXS, spectrophotometry and DLS measurements become invariant with further ripening. All samples have evolved from turbid pink emulsions to clear blue suspensions. We subsequently focused on the PEGX/Y-NPs cluster suspensions, because the control of the PEG-SH ligand grafting onto the gold NP surface is more accurate than that of the adsorption of the PVP chains.

A sample of PEG2000/10-NPs clusters was vitrified as a thin film on a TEM grid and imaged by cryo-TEM. Cryo-TEM was chosen to avoid any deformation due to capillary forces during the solvent drying on the grid in classical TEM experiments. The nanoobjects are indeed imaged within the vitrified liquid. The cryo-TEM micrographs (see an example in Figure 3) show that the objects are dense and globular clusters of NPs, with a submicron size. Their internal structure cannot be fully resolved by TEM due to the large NP density, but it appears very regular, and images of the same object at different tilt angles show no evidence of large voids within the object.

We used SAXS to study the internal structure of the clusters obtained at the end of the ripening as a function of the length and surface density of the organic ligand surrounding the NPs. The ligand molecules help stabilizing the NPs in water and avoid interparticle attraction, which would lead to uncontrolled aggregation, but it is also a lever for controlling the final cluster structure. Figure 4.(a) displays the SAXS signals of three samples with different ligand length: the PEG6000/20-NPs cluster suspension (light blue), the PEG2000/20-NPs cluster suspension (dark blue) and the PEG800/20-NPs cluster suspension (black). They display a clear evolution of the interparticle correlation peak position depending on the length of the NPs ligand, for the same nominal surface density (2 molecules/nm^2) of the ligands on the gold surface: the positions q_1, q_2 and q_3 lead to edge-to-edge distances d_{e-e} of 6.9 nm, 4 nm and 1.9 nm, respectively for the PEG6000/20-NPs, PEG2000/20-NPs and PEG800/20-NPs systems. Figure 4.(b) displays the SAXS signals of three samples with the same ligand length but different nominal densities at the gold surface (PEG2000/20-NPs, light blue; PEG2000/10-NPs, dark blue; and PEG2000/5-NPs, black). Again, we see a clear evolution of the interparticle correlation peak positions q_1, q_2 and q_3 leading to edge-to-edge distances d_{e-e} of 4.4 nm, 2.3 nm and 1 nm, respectively for the PEG2000/20-NPs, PEG2000/10-NPs and PEG2000/5-NPs systems. These values show that the gold NPs get closer to each other within the clusters when the ligand molecules are shorter or less densely grafted at the gold surface. This organic spacer between adjacent nanoparticles is always thick enough to prevent metallic contact and NP fusion[32]. Importantly, the choice of the NPs ligand, which defines the thickness of this spacer, controls the final gold volume fraction within the clusters.

With a packing homogeneous over the whole cluster volume, as suggested by the cryo-TEM results, the obtained center-to-center distances $d_{c-c} = 2\pi/q^*$ can be related to the gold volume fractions f within the clusters, which can be estimated as close to

$$f = p\Psi, \text{ with } \Psi = \left(\frac{2r_s}{d_{c-c}}\right)^3, \tag{3}$$

where p is the packing density of a close-packed sphere assembly and can typically range between 0.64 for moderately polydisperse spheres[33] and 0.74 for monodisperse spheres, and Ψ is the fraction of gold in the volume of the equivalent

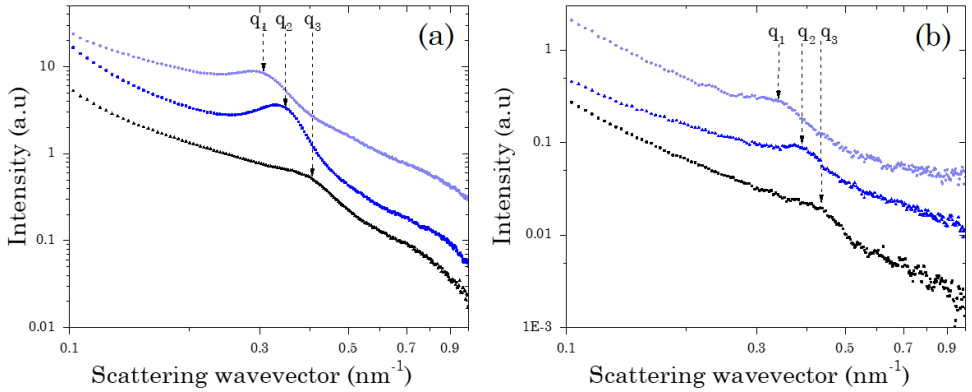

Fig. 4 Study by SAXS of the internal structure after complete ripening as a function of (a) the length and (b) the surface density of the organic ligand grafted onto the NP surface. The curves are vertically shifted for clarity. (a) Interparticle correlation peaks are at positions $q_1 = 0.31$ nm^{-1} (PEG6000/20-NPs, light blue), $q_2 = 0.36$ nm^{-1} (PEG2000/20-NPs, dark blue) and $q_3 = 0.41$ nm^{-1} PEG800/20-NPs, black). (b) Interparticle correlation peaks are at positions $q_1 = 0.35$ nm^{-1} (PEG2000/20-NPs, light blue), $q_2 = 0.40$ nm^{-1} (PEG2000/10-NPs, dark blue) and $q_3 = 0.44$ nm^{-1} (PEG2000/5-NPs, black).

packed spheres (gold + ligand shell).

Table 1 Experimental values of the gold volume fraction f in the clusters as a function of the length and nominal surface density of the PEG-ligands grafted on the gold NPs, when taking the value 0.64 for the packing factor p

f	PEG800	PEG2000	PEG6000
0.5 mol/nm^2	-	0.53	0.24
1 mol/nm^2	-	0.40	-
2 mol/nm^2	0.43	0.27	0.19
4 mol/nm^2	0.46	-	-

The Table 1 gives the values of f obtained from the X-ray study, if we take $p = 0.64$ for all studied samples. The values of the gold volume fraction f, as given by Equation (3) with d_{c-c} extracted from the SAXS measurements, range from $f = 0.19$ for sample PEG6000/20-NPs to $f = 0.53$ for sample PEG2000/5-NPs. Obviously, the cluster density decreases from the top left corner (small ligand quantity) to the lower right corner (large ligand quantity) of the Table 1.

In an effort to maximize the cluster density, we have also formulated the samples PEG800/5-NPs and PEG800/10-NPs, in the upper left corner of the Table 1, but these samples showed no peak or a non-reproducible peak in the SAXS study, which indicated that the ligand quantity surrounding the NPs in the initial emulsions is too low to insure their colloidal stability and thus the regular building up of the clusters. These samples were therefore discarded. On the other hand, we produced clusters corresponding to the opposite (lower right) corner of the Table 1 and lower gold volume fractions, and found them stable. Their optical properties, however, were similar or less interesting than that of the ones described below, due to their lower gold density, and are not detailed here, for conciseness.

Finally, we have demonstrated a fabrication route giving access to NP-clusters of well-controlled structure, presenting gold volume fraction from 20 to more than 50% and in large quantity: one batch of emulsion preparation provides typically 10^9 objects, i.e. enough to cover a surface of ~ 1 cm^2 as a dense cluster monolayer. Such a quantity can be easily upscaled. In order to demonstrate their potential interest in metasurface applications, we have studied their properties of resonant light scattering when varying their internal structure.

2.4 Clusters light scattering properties

We studied the light scattering properties of the clusters in dodecane suspensions using a variable angle polarization resolved static light scattering setup, sketched on Fig. 5. The geometry is the following: the incident white light beam propagates along z and is linearly polarized in the xy plane using P1. The polarization is set at an angle ϕ with respect to the scattering plane yz by rotating a motorized achromatic Fresnel Rhomb tandem (FR). In contrast with the work in Ref. 34, we use a goniometer to measure the scattering across a wide angular range from 20° (forward) to 140° (backward).

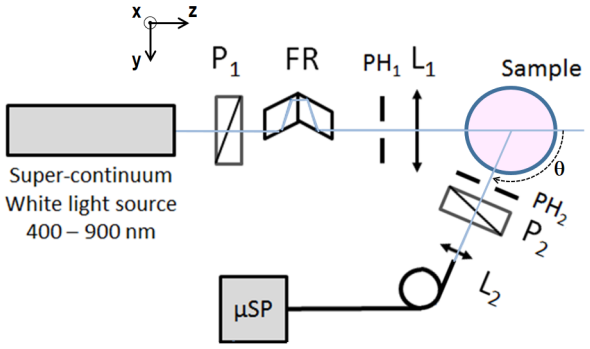

Fig. 5 Static light scattering setup. P_1 and P_2 are broadband polarizers, FR is a Fresnel rhomb tandem, L_1 and L_2 are lenses and PH_1 and PH_2 are pinholes. μSP is a spectrophotometer. θ is the scattering angle and varies from 20 to 140°.

The intensity scattered by the suspension in the yz plane at the angle θ (in the y direction when $\theta = 90°$) is measured by a spectrophotometer through a polarizer (P2) which selects either the horizontal polarization (parallel to the scattering plane yz) $I_{SH}(\phi)$ or the vertical polarization (orthogonal to the scattering plane) $I_{SV}(\phi)$.

The components E_{SH} and E_{SV} of the scattered field at a distance r of the scatterer can be expressed using the matrix formalism[35]:

$$\begin{pmatrix} E_{SH} \\ E_{SV} \end{pmatrix} = \frac{e^{ikr}}{-ikr} \begin{pmatrix} S_2(\theta) & 0 \\ 0 & S_1(\theta) \end{pmatrix} \begin{pmatrix} E_i \sin\phi \\ E_i \cos\phi \end{pmatrix} \tag{4}$$

with k the wavevector and where, for isotropic scatterers, the non-diagonal terms are zero and S_1 and S_2 do not depend on ϕ. The matrix elements $S_1(\theta)$ and $S_2(\theta)$ collect the scattering of the even and odd modes respectively. When $\theta = 90°$, they may be written[36] up to the quadrupole order

$$\begin{cases} S_1(90°) = \frac{3}{2}a_1 - \frac{5}{2}b_2 \\ S_2(90°) = \frac{3}{2}b_1 - \frac{5}{2}a_2 \end{cases} \tag{5}$$

where a_1, a_2, b_1 and b_2 are the Mie scattering coefficients of the electric dipole, electric quadrupole, magnetic dipole and magnetic quadrupole, respectively. For a Huygens scatterer, the scattering of odd and even multipoles should be equal, which translates into the following condition

$$S_1(90°) = S_2(90°) \tag{6}$$

This condition is only rigorous if the series is truncated at the dipole order. If higher order multipoles are significant, the Huygens condition cannot be expressed in terms of $S_1(90°)$ and $S_2(90°)$.

The intensities measured along the two output polarizations for isotropic scatterers then read:

$$\begin{cases} I_{SV} = I_0(\lambda) n_c \sigma_V(90°) \delta\Omega g(\lambda, \delta\Omega) \sin^2\phi = A_V(\lambda) \sin^2\phi \\ I_{SH} = I_0(\lambda) n_c \sigma_H(90°) \delta\Omega g(\lambda, \delta\Omega) \cos^2\phi = A_H(\lambda) \cos^2\phi \end{cases} \tag{7}$$

in which $\sigma_V(90°) = \frac{|S_1(90°)|^2}{k^2}$ is the differential scattering cross-section due to the even multipoles, $\sigma_H(90°) = \frac{|S_2(90°)|^2}{k^2}$ is the one due to the odd multipoles, $I_0(\lambda)$ is the spectral irradiance of the incident beam, n_c is the number of clusters in the scattering volume, and $\delta\Omega$ is the solid angle of the detection window. $g(\lambda, \delta\Omega)$ is an unknown function that accounts for the spectral sensitivity of the detector and optical transmission or reflection of all optical elements. In this last set of equations, A_V and A_H represents the strength of the scattered intensity along the vertical and horizontal output polarizations respectively. Finally, in the dipolar approximation, the Huygens condition expressed by Equation 6 corresponds experimentally to a ratio A_H/A_V as close to unity as possible.

In order to assess the main effects of the gold volume fraction on the scattering properties of the clusters, we may perform a simple calculation assuming monodisperse clusters of radius $R = 100$ nm made of a Maxwell Garnett effective

medium[37] of gold with a volume fraction f and an organic medium of index $n = 1.467$ to account for the ligand molecules, with volume fraction $1 - f$. Following Mie theory, we use the calculated effective index to compute the coefficients a_1, b_1, a_2, b_2, etc., of the clusters. For f values of the order of 0.20, we determine that the quadrupole coefficients a_2 and b_2 are not negligible, but that further modes are (data not shown). The computed theoretical values of the ratio A_H/A_V are shown on Fig. 6.(a) for three values of the volume fraction $f = 0.10$, 0.15 and 0.20.

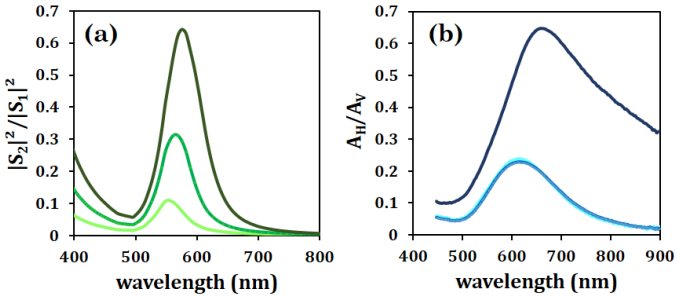

Fig. 6 (a) Calculated ratio of $|S_2(90°)|^2$ and $|S_1(90°)|^2$ at a scattering angle $\theta = 90°$ as a function of wavelength λ for clusters modelled as spheres of effective media using the Maxwell Garnett approximation, with gold volume fraction of 0.10 (light green line), 0.15 (medium green line) and 0.20 (dark green line). (b) Experimental ratio of A_H (intensity measured parallel to the scattering plane) to A_V (intensity measured orthogonal to the scattering plane) as a function of wavelength λ for cluster samples PEG6000/20-NPs (light blue line), PEG2000/20-NPs (medium blue line) and PEG800/40-NPs (dark blue line) at a scattering angle $\theta = 90°$.

Obviously, in this simple model, the increase of the gold volume fraction within the cluster volume induces an increase in the ratio of A_H to A_V, which indicates an evolution towards the Huygens scattering regime of forward-only scattering, as well as a slight red shift of the maximum.

The measured perpendicular and parallel signals $I_{SV}(\phi)$ and $I_{SH}(\phi)$ (shown in the Supplementary Information for sample PEG800/40-NPs at a wavelength of 660 nm) are fitted to simple functions:

$$\begin{cases} I_{SV}(\phi) = A_V \sin^2\phi + B \\ I_{SH}(\phi) = A_H \cos^2\phi + B \end{cases} \tag{8}$$

As shown in the Supplementary Information, the small value of the background signal B crucially validates the assumption of *isotropic* scatterers[38]: the clusters have same resonances for all illumination directions. The values of A_H and A_V are extracted for all studied wavelengths, and their ratio is plotted as a function of wavelength on Fig. 6.(b).

The samples PEG2000/20-NPs and PEG6000/20-NPs, with volume fractions close to 0.2, present the same A_H-to-A_V ratio, culminating at 24%, at $\lambda = 620$ nm. The ratio reaches 65% at $\lambda = 650$ nm for the denser PEG800/40-NPs clusters, which is ≈ 15 times and ≈ 4 times higher than with gold raspberries[34] and gold dodecapods[39], respectively, thus demonstrating the interest of the cluster geometry, in particular for strong optical magnetism. The experimental and numerical results are in qualitative agreement (Figure 6), with both a significant increase of the maximum value of the A_H-to-A_V ratio and a slight red-shift of this maximum with the increasing volume fraction of gold within the clusters. This agreement shows that the simple Maxwell Garnett model grasps the physics of the system. Nevertheless, the amplitude of the ratio peaks is lower, the resonance wavelength is significantly more red-shifted and the spectral width of the curves is larger for the experimental data at all gold volume fractions. This may be related to the experimental distribution of the size and possibly of the internal density of the clusters, and to the fact that the Maxwell Garnett mixing rule fails to describe properly the effective refractive index and the scattering behavior of dense clusters. In particular, the Maxwell Garnett effective medium law neglects plasmonic coupling, which occurs for elevated NP volume fraction and induce red shifts in the resonance signal.

Using normalization with a model dispersion of colloidal silica (of radius 60 nm and narrow size distribution) as described in Ref. 40, we are able to quantitatively extract the differential scattering cross-sections $\sigma_V(90°)$, due to the even multipoles, and $\sigma_H(90°)$, due to the odd multipoles, at $\theta = 90°$ for each sample, shown on Fig. 7.(a)-(c). Their absolute values was extracted from the experimental data using the concentrations n_c of clusters and n_s of reference silica beads in the respective suspensions (see details in the Experimental Section below). Due to the experimental uncertainties on the clusters concentrations ($6.8 \times 10^{10} \leq n_c \leq 8.8 \times 10^{10}$ particles/L), we used the minimum value of the concentration

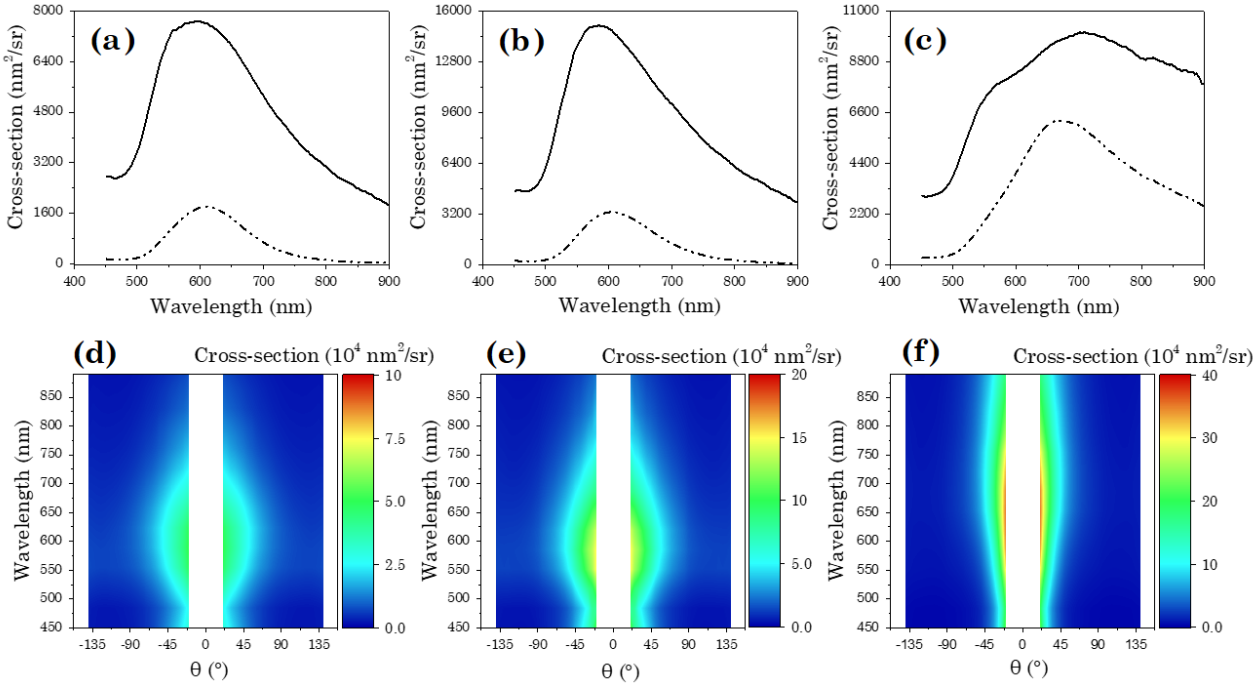

Fig. 7 Upper: Experimental differential scattering cross-sections σ_V (in nm^2/steradian, measured orthogonal to the scattering plane, full line) and σ_H (measured parallel to the scattering plane, dashed line) at the scattering angle $\theta = 90°$. Lower: Experimental scattering patterns: values of the differential scattering cross-section $(\sigma_V(\lambda,\theta)+\sigma_H(\lambda,\theta))$ as a function of the wavelength λ and the scattering angle θ, for cluster samples (a,d) PEG6000/20-NPs (gold volume fraction estimated at $f \approx 0.19$), (b,e) PEG2000/20-NPs ($f \approx 0.27$) and (c,f) PEG800/40-NPs ($f \approx 0.46$). We measured only for $\theta > 0$, but assumed that $\sigma_V(\lambda,-\theta)+\sigma_H(\lambda,-\theta) = \sigma_V(\lambda,\theta)+\sigma_H(\lambda,\theta)$. Note that the nm^2/steradian color scale is enhanced by a factor 2 going from (d) to (e) and by 2 again from (e) to (f).

ratio, $\frac{n_s}{n_c} = 2160$, therefore extracting a *lower bound* of the clusters scattering cross-sections. As shown in Fig. 7.(a)-(c), the differential scattering cross-sections at $\theta = 90°$ increase significantly between the PEG6000/20-NPs clusters (Fig. 7.(a), gold volume fraction $f \approx 0.19$) and the PEG2000/20-NPs clusters (Fig. 7.(b), $f \approx 0.27$). Upon increasing f further to 0.46, σ_H increases strongly (Fig. 7.(c)), reaching towards σ_V. For the higher gold volume fraction, σ_V presents a shoulder at ~ 550 nm, which may be due to the fact that the number of eigenmodes in the structure is increased, each of which may have non-zero coupling to the spherical harmonic vector fields that form the basis of the multipolar decomposition. In fact, simulations show (see Fig. S4) that the electric dipole contribution to the scattering efficiency becomes dual peaked when the gold volume fraction reaches 0.4. We also fully determine the spectral position and relative amplitudes of the two resonant modes. Increasing cluster gold volume fraction f (from left to right on Fig. 7) leads to a red shift, from $\approx$ 590 nm for PEG6000/20-NPs to $\approx$ 670 nm for PEG800/40-NPs, and to a spectral broadening of the resonances.

In order to demonstrate experimentally the forward-scattering property of the clusters, we next moved the sensor to different θ angles between 20° and 140°. For all values of the wavelength λ, we measured the intensities $I_{SV}(\phi,\theta)$ and $I_{SH}(\phi,\theta)$. These measured values were all fitted to Equations (7) and (8), from which we extract $\sigma_V(\lambda,\theta)$ and $\sigma_H(\lambda,\theta)$, using the same normalization with a model dispersion of colloidal silica as before. A lower bound of their absolute values are determined using the minimum ratio of silica to clusters concentrations, as before. Although we cannot measure the scattering at angles below 20° and beyond 140°, the gathered data show the strong directionality of the scattering patterns. The total normalized scattering $(\sigma_V(\lambda,\theta)+\sigma_H(\lambda,\theta))$ is plotted on Figure 7.(d)-(f) for cluster samples PEG6000/20-NPs, PEG2000/20-NPs and PEG800/40-NPs, respectively. As can be seen, the scattering broadens spectrally, increases in strength and is directed towards smaller angles as the cluster density increases (from (d) to (f)), in accordance with an increase of σ_H relative to σ_V (panels (a) to (c)). In particular, sample PEG800/40-NPs (Fig.7.(f)) presents a narrow angle range of strong scattering, which explains that the maximum of σ_V at 90° for this sample is lower than that for the less dense sample PEG2000/20-NPs (Fig. 7.(b) and (c)). The total scattering is also represented on the polar plots of Figure 8.(a) for the cluster samples PEG6000/20-NPs, PEG2000/20-NPs and PEG800/40-NPs, at the wavelength corresponding to the maximum of the A_H/A_V ratio (620, 620 and 650 nm respectively). The computed

scattering for silica beads of same size has to be multiplied by a factor 20 (cyan line on Fig. 8.(a)) to be displayed on the same scale as the clusters scattering. Figure 8.(b) shows the evolution of the PEG2000/20-NPs scattering for three different wavelengths. The scattering increases from 520 to 620 nm, then decreases from 620 to 750 nm, with the highest and most forward scattering occurring at 620 nm where the A_H/A_V ratio is maximum.

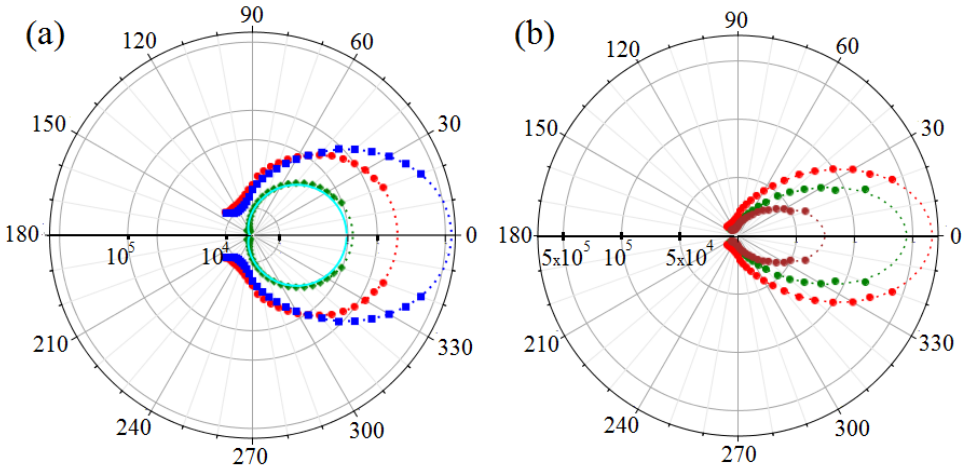

Fig. 8 (a) Logarithmic polar plot of the experimental differential scattering cross-section ($\sigma_V(\theta)+\sigma_H(\theta)$) for the three gold clusters PEG6000/20-NPs (gold volume fraction estimated at $f \approx 0.19$, green diamonds), PEG2000/20-NPs ($f \approx 0.27$, red circles) and PEG800/40-NPs ($f \approx 0.46$, blue squares) recorded at the maximum of the A_H/A_V ratio (620, 620 and 650 nm respectively). The full cyan line is the scattering of a silica nanoparticle of same size ($r_s = 120$ nm) computed from the Mie theory and multiplied by a factor 20 for a better visibility. Note the logarithmic radial scale in nm^2/steradian units. (b) Linear polar plot of the differential scattering cross section for PEG2000/20-NPs ($f \approx 0.27$) recorded at three wavelengths: 520 nm (green circles), 620 nm (the red circles show the same PEG2000/20-NPs data at same wavelength on both polar plots) and 750 nm (brown circles). Note that the highest and most forward scattering occurs at 620 nm where the A_H/A_V ratio is maximum. Dotted lines are guides for the eye.

Both Figures 7 and 8 show that the scattering of the NP-clusters is strongly directed forward and increases in strength as the cluster density increases. Clearly, for the three studied samples, the whole back hemisphere scattering, beyond 90°, is very low compared to the forward scattering (below 90°), and even more so for the denser clusters of sample PEG800/40-NPs.

3 Conclusions

Using wet chemistry, we have produced tailored isotropic colloidal nanoresonators with electric and magnetic resonances engineered so that the resonators act as strong and isotropic Huygens scatterers. The resonators are clusters of gold NPs with radii of approximately 120 nm, in which the gold volume fraction can be varied between typically 20 and 50%, via the tuning of the organic layer grafted around the constitutive NPs. Measuring in a comprehensive manner the light scattering properties of these resonators, dispersed in a solvent, as a function of wavelength and angle, we showed that the volume fraction controls the spectral position and relative strength of the electric and magnetic plasmon-enhanced Mie resonances. The ratio between anti-symmetric (odd) and symmetric (even) modes reaches 65%, far above the values reported in other gold-based nanocolloidal resonators such as plasmonic raspberries (odd/even = 4.5%[34]) or dodecahedral clusters (odd/even = 14%[39]). Moreover, the odd and even resonances are brought into close spectral proximity, which greatly increases the forward-scattering in the visible wavelengths. The densest clusters act as strong Huygens sources, with a dominantly forward scattering in the visible wavelength range, making them excellent candidates for functional meta-devices[3]. While other cluster colloidal assembly routes may be shown in the future to also produce Huygens scatterers, our bottom-up fabrication method based on an initial emulsification process is simple, cost-effective and energy-saving. It is easily scalable for a large-scale production and highly versatile since the clusters can be loaded with any kind of metallic or dielectric nanoparticles for a finer tuning of the optical properties[15]. Changing gold for silver for instance, is expected to further improve the balance between odd and even scattering modes[40], while reducing losses, hence reinforcing the directionality of the scattering.

4 Materials and methods

4.1 Materials

We used a surfactant from the Dow Corning company (with commercial name DC 5225C) that is a mixture of cyclopentasiloxane, poly(ethylene glycol)-*co*-poly(propylene glycol) copolymers and dimethicone. Poly(vinylpyrolidone) (PVP) of molar mass M_w = 10 kg/mol, dodecane and methoxy poly(ethylene glycol) thiol (PEG-SH) monofunctional polymers of molar mass M_w = 800 g/mol, 2000 g/mol and 6000 g/mol were purchased from Aldrich. All products were used as received without further purification.

4.2 Gold nanoparticle suspensions

In order to prepare the emulsion dispersed phase, citrate-coated gold NPs were first synthesized in water at a volume fraction of 2.5×10^{-6} following the Turkevitch method[41,42]. Citrate was then replaced with polymers, thus producing different gold NP samples. In a first experiment, poly(vinylpyrolidone) (M_w = 10 kg/mol) was adsorbed on the gold NPs, giving the suspension referred to as PVP-NPs. In a second experiment, three methoxy poly(ethylene glycol) thiols (PEG-SH) of molar mass M_w = 800 g/mol, 2000 g/mol and 6000 g/mol were grafted on the gold NPs. The grafting process involved adding a quantity α (mol) of PEG-SH to the aqueous suspension of citrate-coated gold NPs, so that $\frac{\alpha N_A}{4\pi n_P r_s^2}$ is the nominal grafting density at the gold surface, with N_A the Avogadro number, n_P the number of NPs in the suspension and r_s the mean radius of the gold NPs. Several suspensions were produced with the different PEG-SH ligands and different nominal densities between 0.5 and 4 ligand molecules/nm^2, giving the suspensions referred to as PEGX/Y-NPs, where, as explained before, X is the molar mass of the PEG-SH and Y is 10 times the number of ligand molecules/nm^2. For instance, PEG2000/20-NPs is produced with the PEG-SH of length M_w = 2000 g/mol at a nominal density of 2 molecules/nm^2. All suspensions were thoroughly washed (using centrifugation cycles), in order to remove displaced citrate and sodium ions, as well as any polymer in excess.

4.3 Emulsions

The PVP-NPs, and several PEGX/Y-NPs aqueous suspensions were each emulsified in dodecane at a concentration of 20 vol% using an Ultraturax mixer with DC 5225C as surfactant (at a concentration of 10 wt% in the dodecane).

4.4 Structural studies

4.4.0.1 Infrared spectroscopy. Infra-red spectroscopy in the ATR-FTIR mode was performed using a Nicolet 6700 spectrometer Thermo Scientific equipped with a MCT detector cooled at 77K. The IR radiation is directed on a germanium crystal at an incidence angle $\phi = 45°$, below the critical angle. The reflection creates an evanescent wave, which travels beyond the surface of the crystal and penetrates through the sample placed on the surface. The depth of penetration is given by:

$$d_p = \frac{\lambda}{2\pi n_1 \sqrt{\sin^2(\phi) - (\frac{n_2}{n_1})^2}}$$

where, λ denotes the wavelength, n_1 and n_2 are the refractive indices of the germanium crystal and the sample respectively. The d_p was calculated to be 0.14 μm at λ = 2.873 μm. For each spectrum, 200 scans were recorded at a resolution of 8 cm^{-1}.

4.4.0.2 UV-visible spectroscopy The measurements were carried out using a UV-Visible Jasco V-730 spectroscope in the wavelength range from 350 to 800 nm. The cluster suspensions were studied in PMMA cells with a 1 cm optical path and a pure solvent cell was used as a reference.

4.4.0.3 Size measurements by light scattering Dynamic light scattering (DLS) measurements, giving access to the analysis of the translational diffusion of scatterers in suspension in a solvent, were performed using an ALV laser goniometer, with a 632.8 nm HeNe linearly polarized laser and an ALV-5000/EPP multiple tau digital correlator. The DLS autocorrelation functions were obtained at scattering angles of 60°, 90° and 120° at a temperature of 25°C. The time decay of the autocorrelation functions was found not to be a perfect monoexponential and could be fitted by a second-order cumulant expansion[43], giving access to a log-normal size distribution for the scatterers radius. Granulometry, with a

Malvern Nano-ZS, was used for the measurement of the initial emulsion droplet size distribution, as they were too turbid to be studied with the DLS setup.

4.4.0.4 Cryogenic Transmission electron microscopy (Cryo-TEM). Samples for cryo-TEM imaging were prepared using a fully automated vitrification device (Leica, EM GP). First, 3 μL of the cluster suspension in dodecane was deposited onto a glow discharged 300 Mesh Cu grid covered with a lacey-carbon film (Ted Pella, 01883-F). The grid was then mechanically blotted and immediately plunged into liquid nitrogen in order to vitrify the dodecane. The frozen grid was mounted in a Gatan cryo-TEM holder, and examined at low dose below -175°C in a FEI Talos S200C microscope operated at 200 kV. Images were collected using a Ceta camera ($4k \times 4k$) and analyzed using Digital Micrograph Gatan Inc. software.

4.4.0.5 Small-angle X-ray scattering. SAXS profiles were acquired in transmission on a XEUSS device (Xenocs) with a microfocus copper anode source, a scatterless collimation system and a PILATUS 2-D detector, giving access to scattering wavevector q values from 0.08 to 8 nm^{-1}. The cluster suspensions were put in thin glass capillaries. The resulting 2D images were found to be isotropic, and the data were azimuthally averaged to yield the scattering curve of the intensity $I(q)$, corrected from experimental background, versus $q = (4\pi/\lambda)\sin\theta$, where $\lambda = 0.154$ nm is the wavelength of the Cu $K\alpha$ radiation and θ is half the scattering angle.

4.5 Static polarization-resolved spectroscopic light scattering measurements

A static light scattering (SLS) set-up including a supercontinuum white source (SuperK EXB-6 with SuperK Split UV-visible filter from NKT Photonics) was used to deliver a light beam covering the 400-850 nm wavelength range and shone onto a dilute dodecane suspension of scatterers (see Fig. 5). The linear polarization of the incident light is defined by the angle ϕ (ϕ=0 when the electric field is along y), which was rotated in steps of 10° by a Fresnel Rhomb tandem (Thorlabs FR600HM) mounted on a rotation stage. The polarization of the scattered light was analyzed by a Glan-Taylor polarizer (Thorlabs GL5-A) set perpendicular (V) or parallel (H) to the scattering plane. The scattered light was collected through a collimated fiber (NA = 0.25) by a spectrometer (Hamamatsu C10083CA) mounted on a goniometer, in order to span scattering angles θ from 20 to 140°, in steps of 5°. Due to mechanical constraints on the one hand, and the impossibility to measure close to the direct beam at $\theta = 0$, on the other hand, no measurements were made below 20° and beyond 140°. An aqueous suspension of silica particles of radius 60 nm and narrow size distribution, with a NP density $n_s = 2.1 \pm 0.2 \times 10^{14}$ particles/L, was used as a reference. A good agreement of the experimental ratio of A_H to A_V for the silica reference at a few test wavelengths $\lambda = 550$, 600 and 700 nm, with a $\cos^2\theta$ function, demonstrates the good alignment of the goniometer (data not shown). The clusters suspensions were diluted before measurements, and the final concentrations n_c were all verifying $6.8 \times 10^{10} \leq n_c \leq 8.8 \times 10^{10}$ particles/L.

Conflicts of interest

There are no conflicts to declare.

Acknowledgements

This work was performed within the framework of the LabEx AMADEus ANR-10-LABEX-0042-AMADEUS with the help of the French state Initiative d'Excellence IdEx ANR-10-IDEX-003-02. We acknowledge the help of Isabelle Ly from CRPP. We thank Laurent Lermusiaux, from ICMCB, for providing the reference silica beads and Gaëlle Trézéguet, from UNIVAR, for providing the DC surfactant.

References

1 K. Chen, Y. Feng, F. Monticone, J. Zhao, B. Zhu, T. Jiang, L. Zhang, Y. Kim, X. Ding, S. Zhang *et al.*, *Advanced materials*, 2017, **29**, 1606422.

2 G. M. Akselrod, J. Huang, T. B. Hoang, P. T. Bowen, L. Su, D. R. Smith and M. H. Mikkelsen, *Advanced Materials*, 2015, **27**, 8028–8034.

3 R. Dezert, P. Richetti and A. Baron, *Optics express*, 2019, **27**, 26317–26330.

4 L. Wang, S. Kruk, H. Tang, T. Li, I. Kravchenko, D. N. Neshev and Y. S. Kivshar, *Optica*, 2016, **3**, 1504–1505.

5 S. Kruk, B. Hopkins, I. I. Kravchenko, A. Miroshnichenko, D. N. Neshev and Y. S. Kivshar, *Apl Photonics*, 2016, **1**, 030801.

6 M. Decker, I. Staude, M. Falkner, J. Dominguez, D. N. Neshev, I. Brener, T. Pertsch and Y. S. Kivshar, *Advanced Optical Materials*, 2015, **3**, 813–820.

7 A. Tittl, A. Leitis, M. Liu, F. Yesilkoy, D.-Y. Choi, D. N. Neshev, Y. S. Kivshar and H. Altug, *Science*, 2018, **360**, 1105–1109.

8 K. Fan, J. Zhang, X. Liu, G.-F. Zhang, R. D. Averitt and W. J. Padilla, *Advanced Materials*, 2018, **30**, 1800278.

9 M. Liu and D.-Y. Choi, *Nano letters*, 2018, **18**, 8062–8069.

10 C. Huygens, *Traité de la lumière:...*, chez Pierre vander Aa, marchand libraire, 1920.

11 I. Staude, A. E. Miroshnichenko, M. Decker, N. T. Fofang, S. Liu, E. Gonzales, J. Dominguez, T. S. Luk, D. N. Neshev, I. Brener and Y. Kivshar, *ACS Nano*, 2013, **7**, 7824–7832.

12 R. Alaee, R. Filter, D. Lehr, F. Lederer and C. Rockstuhl, *Optics letters*, 2015, **40**, 2645–2648.

13 A. Baron, A. Aradian, V. Ponsinet and P. Barois, *Optics & Laser Technology*, 2016, **82**, 94–100.

14 V. Ponsinet, A. Baron, E. Pouget, Y. Okazaki, R. Oda and P. Barois, *EPL (Europhysics Letters)*, 2017, **119**, 14004.

15 R. Dezert, P. Richetti and A. Baron, *Physical Review B*, 2017, **96**, 180201.

16 C. Rockstuhl, F. Lederer, C. Etrich, T. Pertsch and T. Scharf, *Physical Review Letters*, 2007, **99**, 017401.

17 S. Mühlig, C. Rockstuhl, V. Yannopapas, T. Bürgi, N. Shalkevich and F. Lederer, *Optics Express*, 2011, **19**, 9607.

18 J. Dintinger, S. Mühlig, C. Rockstuhl and T. Scharf, *Optical Materials Express*, 2012, **2**, 269.

19 C. Durand-Gasselin, N. Sanson and N. Lequeux, *Langmuir*, 2011, **27**, 12329–12335.

20 J. He, X. Huang, Y.-C. Li, Y. Liu, T. Babu, M. A. Aronova, S. Wang, Z. Lu, X. Chen and Z. Nie, *Journal of the American Chemical Society*, 2013, **135**, 7974–7984.

21 A. Sánchez-Iglesias, M. Grzelczak, T. Altantzis, B. Goris, J. Pérez-Juste, S. Bals, G. Van Tendeloo, S. H. Donaldson, B. F. Chmelka, J. N. Israelachvili and L. M. Liz-Marzán, *ACS Nano*, 2012, **6**, 11059–11065.

22 A. K. Boal, F. Ilhan, J. E. DeRouchey, T. Thurn-Albrecht, T. P. Russell and V. M. Rotello, *Nature*, 2000, **404**, 746–748.

23 J.-F. Berret, *Advances in Colloid and Interface Science*, 2011, **167**, 38–48.

24 Q. Yin, X. Han, V. Ponsinet and H. Liu, *Journal of Colloid and Interface Science*, 2014, **431**, 97–104.

25 V. N. Manoharan, M. T. Elsesser and D. J. Pine, *Science*, 2003, **301**, 483–487.

26 Y.-S. Cho, G.-R. Yi, S.-H. Kim, D. J. Pine and S.-M. Yang, *Chemistry of Materials*, 2005, **17**, 5006–5013.

27 H. K. Yu, G.-R. Yi, J.-H. Kang, Y.-S. Cho, V. N. Manoharan, D. J. Pine and S.-M. Yang, *Chemistry of Materials*, 2008, **20**, 2704–2710.

28 J. Lacava, P. Born and T. Kraus, *Nano Letters*, 2012, **12**, 3279–3282.

29 J. Schmitt, S. Hajiw, A. Lecchi, J. Degrouard, A. Salonen, M. Impéror-Clerc and B. Pansu, *The Journal of Physical Chemistry B*, 2016, **120**, 5759–5766.

30 I. Hussain, H. Zhang, M. Brust, J. Barauskas and A. I. Cooper, *Journal of colloid and interface science*, 2010, **350**, 368–372.

31 M. Lin, H. Lindsay, D. Weitz, R. Ball, R. Klein and P. Meakin, *Nature*, 1989, **339**, 360–362.

32 W. Chen, J. Guo, Q. Zhao, P. Gopalan, A. T. Fafarman, A. Keller, M. Zhang, Y. Wu, C. B. Murray and C. R. Kagan, *ACS nano*, 2019, **13**, 7493–7501.

33 R. S. Farr and R. D. Groot, *The Journal of chemical physics*, 2009, **131**, 244104.

34 V. Ponsinet, P. Barois, S. M. Gali, P. Richetti, J.-B. Salmon, A. Vallecchi, M. Albani, A. Le Beulze, S. Gomez-Grana, E. Duguet *et al.*, *Physical Review B*, 2015, **92**, 220414.

35 N. L. Sharma, *Physical Review Letters*, 2007, **98**, 217402.

36 C. F. Bohren and D. R. Huffman, *Absorption and scattering of light by small particles*, John Wiley & Sons, 2008.

37 J. M. Garnett, *Philosophical Transactions of the Royal Society of London. Series A, Containing Papers of a Mathematical or Physical Character*, 1904, **203**, 385–420.

38 S. Gomez-Graña, M. Treguer-Delapierre, E. Duguet, J.-B. Salmon, J. Leng, V. Kravets, A. N. Grigorenko, A. Peyyety, V. Ponsinet, P. Richetti *et al.*, 2016 10th International Congress on Advanced Electromagnetic Materials in Microwaves and Optics (METAMATERIALS), IEEE, 2016, pp. 52–54.

39 V. Many, R. Dézert, E. Duguet, A. Baron, V. Jangid, V. Ponsinet, S. Ravaine, P. Richetti, P. Barois and M. Tréguer-Delapierre, *Nanophotonics*, 2019, **8**, 549–558.

40 S. Gomez-Graña, A. Le Beulze, M. Treguer-Delapierre, S. Mornet, E. Duguet, E. Grana, E. Cloutet, G. Hadziioannou,

J. Leng, J.-B. Salmon, V. G. Kravets, A. N. Grigorenko, N. A. Peyyety, V. Ponsinet, P. Richetti, A. Baron, D. Torrent and P. Barois, *Materials Horizons*, 2016, **3**, 596–601.

41 J. Turkevich, P. C. Stevenson and J. Hillier, *Discussions of the Faraday Society*, 1951, **11**, 55.

42 G. Frens, *Nature Physical Science*, 1973, **241**, 20–22.

43 P. Fabre, C. Quilliet, M. Veyssié, F. Nallet, D. Roux, V. Cabuil and R. Massart, *EPL (Europhysics Letters)*, 1992, **20**, 229.